

COMMUNICATION

Probing compositional engineering effects on lead-free perovskite-inspired nanocrystal thin films using correlative nonlinear optical microscopy

Received 00th January 20xx,
Accepted 00th January 20xx

Shambhatee Annurakshita,^a Maning Liu,^{b,c,d} Paola Vivo,^b and Godofredo Bautista*^a

DOI: 10.1039/x0xx00000x

We introduce the use of correlative third-harmonic generation and multiphoton-induced luminescence microscopy to investigate the impact of manganese (Mn) doping to bismuth (Bi)-based perovskite-inspired nanocrystal thin films. The technique was found to be extremely sensitive to the microscopic features of the perovskite film and its structural compositions, allowing the unambiguous detection of compositionally different emitters in the perovskite film and manipulation of their nonlinear optical responses. Our work unveils a new way to investigate, manipulate, and exploit perovskite-inspired functional materials for nonlinear optical conversion at the nanoscale.

The hierarchical nature and heterogeneity of perovskite-inspired architectures strongly impact its optoelectronic performance.¹ For example, thin films of perovskite nanocrystals (NC), which exhibit inherently high surface-to-volume ratios and tunable geometrical properties, are becoming vital in improving stabilities and lowering defect densities in emerging perovskite-inspired architectures.² Compositional engineering,³ surface passivation,⁴ and defects control⁵ have been shown to influence greatly the functionality and performance of perovskite derivatives. To identify the roles of perovskite constituents and their collective contributions to the overall performance of the perovskite architectures, various characterization and imaging techniques are required. Frequently employed techniques for structural evaluation of perovskites include X-ray diffraction (XRD),⁶ scanning electron microscopy (SEM),⁷ transmission electron microscopy (TEM),⁸ and atomic force microscopy (AFM).⁹ Although these techniques can delineate the morphological and atomic features of perovskites at ultrahigh spatial

resolutions, these methods are depth discrimination-limited (i.e., surficial), generally destructive, and requiring special resources (e.g., synchrotron) and extreme environments, making them unsuitable for investigating perovskites noninvasively and/or in operation. Due to these drawbacks, optical imaging techniques, e.g., Raman scattering and photoluminescence (PL), are becoming relevant, providing new insights into the role of perovskite constituents and their interactions with the overall perovskite architecture at multiple length scales. Relying on single-photon based linear scattering or absorption phenomena, these approaches proved to be useful to study the effects of perovskite crystallographic symmetries,¹⁰ band structures and recombination kinetics.¹¹ However, these techniques generate a lot of unwanted background signals that preclude the investigation of spatially localized emitters or important light-matter interaction sites within the volume of the perovskite-based architecture.

Nonlinear optical (NLO) phenomena imbue optical sectioning capabilities to imaging techniques allowing the characterization of nanostructures at high spatial resolution and in a noninvasive way.¹² These techniques are strongly dependent on the material symmetries and the excitation fields. Previous works have revealed the exceptionally high nonlinear absorption coefficients of perovskites,^{13–16} providing a strong basis for studying the spatially resolved multiphoton absorption-induced luminescence (MPL) from many forms of these materials. For example, MPL microscopy is an emerging technique to examine the optical quality (i.e., homogeneity and heterogeneity) of perovskite materials at high spatial resolution,^{17–19} and provide unprecedented spatial localization of trap-states and carrier dynamics within the perovskite material that cannot be depth-resolved by its single-photon imaging counterpart.^{20,21} Equally important nonlinear phenomena that do not rely on absorption effects have been discovered in perovskites,²² allowing additional modifications in their overall optoelectronic performance. Third-harmonic generation (THG) is a high order optical process that involves the conversion of three photons at the fundamental frequency into a single-photon at the third-harmonic frequency. Although THG is not inhibited by strict phase-matching

^a Photonics Laboratory, Physics Unit, Tampere University, Korkeakoulunkatu 3, 33720, Tampere, Finland. Email: gsbautista1@gmail.com

^b Hybrid Solar Cells, Faculty of Engineering and Natural Sciences, Tampere University, P.O. Box 541, FI-33014 Tampere, Finland

^c Centre for Analysis and Synthesis, Lund University, P.O. Box 124, 22100 Lund, Sweden

^d Wallenberg Initiative Materials Science for Sustainability, Department of Chemistry, Lund University, 22100 Lund, Sweden

conditions and wavelength effects, THG will not occur when a beam is focused inside a homogenous normally dispersive medium.²³ Significant THG can only occur when there is an inhomogeneity such as an interface within the focal volume, allowing the unambiguous detection and imaging of nanomaterials.^{24,25} Thanks to the high magnitude of $\chi(3)$ in perovskites that are comparable to those in organic materials,^{26–30} the possibility to investigate, image and control the THG efficiency from various forms of perovskites is being actively pursued.^{31–34}

Due to the hierarchical nature of perovskite-like architectures, there is increasing value in using complementary (or multimodal) imaging techniques to investigate their properties.³⁵ Correlated microscopies of certain portions of the perovskite material provided by different experimental setups have been attempted to identify possible recombination sites, heterogeneity and diffusion in perovskites and their related photon statistics.^{36–40} A major drawback of doing serial imaging with setups that require typically different imaging conditions, however, is having potential errors in imaging of the same areas of interest and most importantly, sample cross-contamination during turnover. Therefore, it is important to develop direct and complementary techniques for noninvasive and correlative light-based characterization and imaging of perovskite derivatives. Here, we introduce the use of correlative NLO microscopy as a new technique to visualize the microscopic properties of bismuth (Bi)-based perovskite-inspired $\text{Cs}_3\text{Bi}_2\text{I}_9$ NC thin films. The technique is based on correlative point scanning and point detection of optical yet spectrally distinct THG and MPL signals from the same region of interest. Especially, we use this technique to probe the impact of manganese (Mn) doping in $\text{Cs}_3\text{Bi}_2\text{I}_9$ NCs to its nonlinear response. THG maps directly reveal inhomogeneities of the NC film. Importantly, the THG signals from Mn doped samples are found to be strongly modulated by the amount of Mn doping. MPL maps at different spectral bands reveal the formation of low-density micron-scale-sized aggregates in Mn doped perovskites. Our work highlights the emerging importance of developing correlative NLO imaging techniques for studying the hierarchical properties of novel perovskite derivatives and manipulating nanoscale NLO phenomena in these kinds of materials.

To examine the NC samples, we used a custom point scanning and point detection nonlinear microscopy setup (Fig. 1a). In the past, we have used this microscope to investigate NLO effects in a variety of nanostructures.^{41–43} Briefly, a femtosecond laser (wavelength 1060 nm, repetition rate 80 MHz, pulse length 140 fs) was used as excitation source. The laser beam output was spatially filtered, expanded, and directed towards a high numerical aperture microscope objective (Nikon CFI LU Plan Fluor Epi P, NA 0.8, magnification 50 \times), which was then used to focus light onto the sample mounted on a piezoscanner. The backscattered signals from the sample were collected using the same objective and steered towards two identical photomultiplier tubes (PMT, PMC-100-0, Becker & Hickl). To distinguish the NLO signal wavelengths from the fundamental wavelength and unwanted background, a longpass filter (FELH0750, Thorlabs) was used in the excitation arm, and appropriate dichroic (FF409-Di03-25x36, Semrock), shortpass (BSP01-785R-25, Semrock) and bandpass (Semrock) filters were used in the detection arms. In one PMT, the following bandpass filters were used: FF02-320/40-25, FF01-356/30-25, and FF01-385/26-25.

In the other PMT, these bandpass filters were used: FF01-500/15-25, FF01-532/18-25, and FF01-560/14-25. Using suitable filter combinations, the detectable signal levels without the sample, i.e., background, were found to be about <20 counts per second (cps) for each PMT channel.

To construct a scanning map, the NLO signals were acquired as function of the sample or motor position using a custom LabVIEW program. A white light source in tandem with a camera was used to select the region of interest in the sample. All nonlinear experiments were done at room temperature and using incident linear polarization (or along y in NLO scanning maps), 50 ms pixel dwell time, and 100 \times 100 pixels resolution. To prevent sample damage, average power of 3 mW as measured before the objective was used. This power setting was verified using independent measurements, in which repeated scanning did not show significant degradation of signals from the sample under NLO and bright-field mapping operations. Image plotting and processing of the raw data were performed using MATLAB. To represent the total MPL map of the sample, the individual MPL maps taken using different bandpass filters (except THG) were added pixel-wise. To show THG and MPL signals in the same picture, corresponding THG and MPL maps were plotted as 8-bit green (G) and red (R) color maps, respectively. Excluding the blue (B) color, the G and R color maps were added pixel-wise, and the result was recomposed as a 24-bit RGB (color space) or “THG+MPL” map.

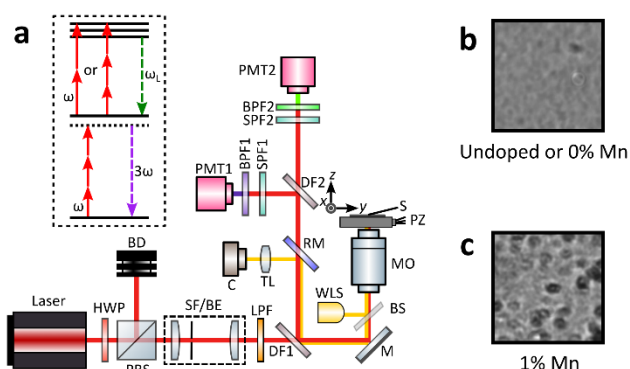


Fig 1 a) Schematic diagram of the NLO scanning microscope with the following components: femtosecond laser, half-wave plate (HWP), polarizing beamsplitter (PBS), beam dump (BD), spatial filter (SF), beam expander (BE), longpass filter (LPF), dichroic filter (DF), mirror (M), microscope objective (MO), piezoscanning system (PZ), sample (S), white light source (WLS), beamsplitter (BS), removable mirror (RM), tube lens (TL), camera (C), shortpass filter (SPF), bandpass filter (BPF), photomultiplier tube (PMT). Inset: Energy diagrams of THG and MPL processes. Depending on the nature of the scattering or absorption, multiple photons at the fundamental frequency ω are converted to a single photon at the THG (3ω) or photoluminescence (ω_i) frequencies. Typical brightfield microscopy images of 10 μm -sized square areas of b) Mn-free or undoped or 0% Mn and c) 1% Mn doped $\text{Cs}_3\text{Bi}_2\text{I}_9$ samples on glass substrate.

The perovskite-inspired materials used in this work are composed of $\text{Cs}_3\text{Bi}_2\text{I}_9$ NCs of varying Mn content. These samples have been synthesized and reproduced using the procedure found in a previous report.⁴⁴ Briefly, in a hot-injection synthesis, 0.1 mmol of BiI_3 , varied amounts of MnI_2 (0, 0.025, 0.05, 0.1, or 0.2 mmol, 4 mL of octadecene, 0.5 mL of oleic acid, and 0.5 mL of oleylamine were mixed into a 25 mL three-neck flask and degassed under vacuum for 1 h at 120 $^\circ\text{C}$. Then, the fully dissolved solution was heated to 160 $^\circ\text{C}$ under Ar gas flow, and 1 mL of Cs-oleate solution (0.075 mmol) was

swiftly injected. The reaction was kept at the injection temperature for 30 s before an ice-cold water bath was set under the three-neck flask. After cooling down to room temperature, the orange crude solution was added with an equal volume of 2-propanol to remove the unreacted precursors and by-products prior to the centrifugation at 4500 rpm for 10 min. After discarding the supernatant, the precipitation (as-synthesized $\text{Cs}_3\text{Bi}_2\text{I}_9\text{:Mn}$ NCs) was redispersed in 5 mL hexane to obtain the pure product. The Mn doping was performed by varying concentration from 0 to 100% mol%. The actual concentration of Mn was estimated using inductively coupled

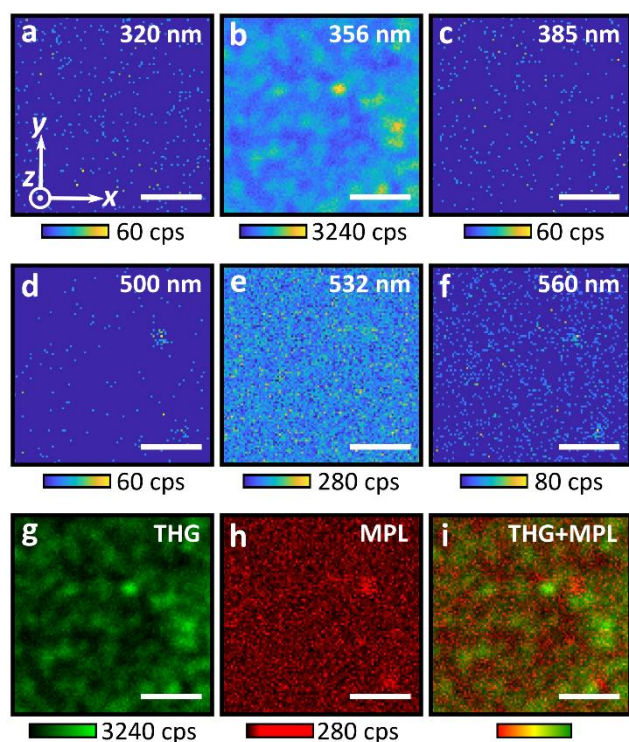


Fig 2 a–f) NLO scanning maps of the undoped $\text{Cs}_3\text{Bi}_2\text{I}_9$ NCs using different bandpass filters. The central wavelengths of the filters are shown in the top-right. g) THG map in b) as an 8-bit green color map. h) Summed MPL map using a,c,d-f) as an 8-bit red color map. i) Composite map of g) and h). The scale bar is 3 μm .

plasma mass spectrometry (ICP-MS) and presented as percentage weight ratio with respect to Bi. Mn doped perovskite samples with different concentrations (0%, 1%, 3%, 5% and 6%) were synthesized. The physical properties (e.g., band structure, molecular composition) of the resulting NCs have been investigated previously.⁴⁴ For example, direct compositional mapping of the representative clusters of the 5% Mn doped NCs revealed that the Mn was incorporated well and distributed evenly into the host NCs. A typical $\text{Cs}_3\text{Bi}_2\text{I}_9\text{:Mn}$ NC thin film was prepared by drop-casting the $\text{Cs}_3\text{Bi}_2\text{I}_9\text{:Mn}$ NC suspension in hexane onto a microscopy glass slide and fully dried in air. This sample configuration is not only fitting to our nonlinear microscopy workstation but also represents a relevant system for solar cell applications. Examination of such drop-casted perovskites on suitable substrates has been found to be practical and economical.⁴⁵ Typical brightfield microscopy images of the prepared 0% and 1% Mn doped samples are shown in Fig. 1b,c.

For reference, we first examined a microscopic area in the undoped or 0% Mn NC sample (Fig. 1b). Representative bandpass-filtered NLO maps of the same area are shown in Fig. 2a–f. NLO signals were found and significant only when the filtered signals are near the expected THG wavelength of ~ 355 nm. The very low NLO signals acquired using the other bandpass filters near the expected THG wavelength further validates that the acquired signals are THG. These signals possibly originate from inhomogeneities within the sample that are comparable to the size of the beam focus. Since the size of the focused beam is always fixed in the NLO experiments, the variations in the THG signal can be directly associated with discrepancies in the size, density, and interface orientations of the NC aggregates within the focal volume. The regions in the THG map

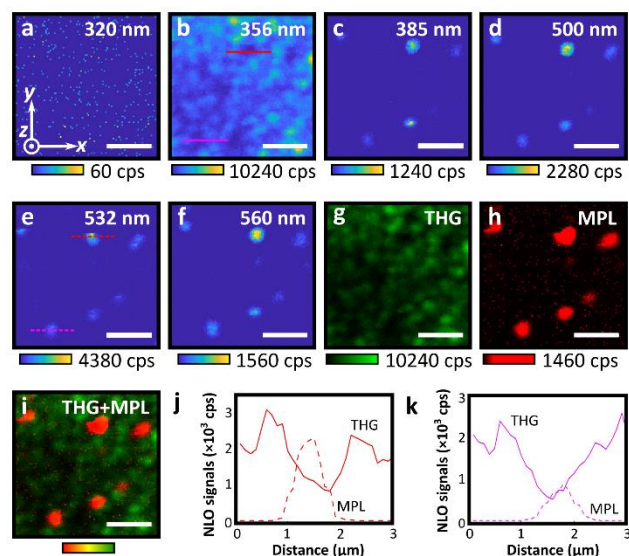


Fig 3 a–f) NLO scanning maps of the 1% Mn doped $\text{Cs}_3\text{Bi}_2\text{I}_9$ NCs using different bandpass filters. The central wavelengths of the bandpass filters are shown in the top-right. g) THG map in b) as an 8-bit green color map. h) Summed MPL map using a,c,d-f) as an 8-bit red color map. i) composite map of g) and h). The scale bar is 3 μm . j,k) NLO signal intensity profiles of the THG and MPL signals that are color-marked in b) and e) showing that the THG and MPL signals are not spatially overlapping.

that have small or close to background signals levels indicate regions that are homogenous, e.g., symmetrically illuminated isotropic NC or air. Since there is no source of symmetry breaking along the optical axis, farfield THG is destructive because of the beam's Gouy phase behavior before and after focusing.²³ As shown in Fig. 2g–i, the NLO signals from the undoped sample are dominated by THG and free from any MPL.

Next, the NLO maps from a microscopic area in the 1% Mn doped $\text{Cs}_3\text{Bi}_2\text{I}_9$ sample (Fig. 1c) are presented. These maps revealed spectrally distinct and spatially varying NLO signals within the same scanning area (Fig. 3a–f). Similar to the results about THG from undoped samples, THG signals from the 1% Mn doped samples were validated near the expected THG wavelength and exhibited variations that are attributed to sample inhomogeneities (Fig. 3b,g). However, the scanning maps taken at other bandpass filters (Fig. 3c–f,h) revealed the presence of localized and nonvanishing NLO signals within the same scanning area. Despite the significantly low absolute photoluminescence yield of these samples, i.e., <2%, the acquired NLO signals possibly represent MPL signals from large micron-sized aggregates in the film that might have been created during the

sample preparation, e.g., stacking of larger-sized hexagonal nanoplatelets, which has been previously observed when doping Mn to the host $\text{Cs}_3\text{Bi}_2\text{I}_9$ NCs.⁴⁴ Although the detection range of the NLO microscope is limited, the high similarity of MPL maps indicates that the MPL emissions from these aggregates are broad and must be associated with certain optical transitions allowed in the material. Furthermore, the MPL hotspots do not spatially overlap with the THG hotspots in the same scanning area (Fig. 3i). In particular, corresponding line profiles of the NLO signals from representative MPL sources clearly show that the MPL and THG signals have different origins (Fig. 3j,k). Within these regions, the THG is possibly coming from the interface of the MPL-active aggregates and host NC aggregates. MPL, on the other hand, mostly comes from the bulk of the large micron-sized aggregate, a direct confinement effect provided by multiphoton excitation that is not accessible in single-photon photoluminescence. Most importantly, the lack of THG within the MPL emitter suggests that the MPL emitter is optically isotropic. This further emphasizes that the prepared sample contains MPL and THG emitting entities that have different photophysical properties, hence different molecular composition. However, the exact origin of the MPL-active emitters in this sample cannot be verified at this time and requires further investigation.

It is well-known that Mn doping affects strongly the photophysical properties (e.g., band structure, emission, and stability) of host semiconductor and perovskites NCs.^{46–49} To date, the identification of the perovskite NC aggregates and byproducts of synthesis in a thin film remains a big challenge even with traditional structural imaging techniques. Furthermore, traditional photoluminescence-based techniques to examine the photophysical properties of such perovskites rely on ensemble measurements that do not provide 3D microscopic and spatial localization of the respective emitters. Direct comparison of our NLO microscopic investigations in the undoped and 1% Mn doped perovskites unambiguously revealed the microscopic yet significant effect of Mn doping in these samples. Our correlative NLO mapping technique directly showed the presence of distinct THG and MPL emitting entities in the film with low dopant level. In this context, high spatial resolution NLO mapping combined with high resolution spectroscopy might find importance in disentangling the origin of the photoluminescence features of a single Mn doped perovskite NC or an equivalent system that remains challenging to extract in ensemble measurements. Due to averaging effects, the features of the photoluminescence spectra might originate from independent and noninteracting populations of emitters within the sample that do not even exhibit competition in energy transfer.

To investigate the role of Mn doping in $\text{Cs}_3\text{Bi}_2\text{I}_9$ NC films to its NLO response, microscopic regions of the 3%, 5% and 6% Mn doped perovskites NC samples (Fig. 4a,e,i) were further examined. The THG and MPL maps from the 3% Mn doped sample (Fig. 4b-d) exhibited NLO signatures and microscopic features that are qualitatively like the results from the 1% Mn doped sample, validating THG and at the same time, revealing the distinct and spatially distinct MPL activity from micron-sized aggregates produced at this dopant level. These results also revealed that the average THG signal levels from the 3% Mn containing sample is higher than those from its 1% counterpart. The notable increase in THG signal levels is suggesting that the 1% and 3% Mn doped NCs exhibit subtle physical differences at the

nanoscale (e.g., size and shape including orientation of interfaces) but strongly impacted their farfield THG responses. Interestingly, the NLO maps of the 5% Mn doped sample (Fig. 4f-h) revealed the formation of significant THG and MPL emitters in microscopic regions within the perovskite NC film. Most interestingly, the composite map (Fig. 4h) showed regions with overlapping THG and MPL activities (seen as yellow) that are not exhibited by those results from the low dopant samples. Essentially, the colocalization of THG and MPL activities within the microscopic MPL emitters strongly suggests that

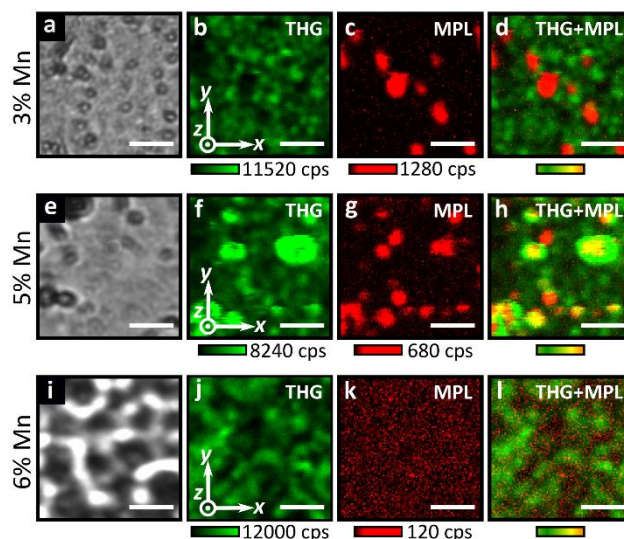


Fig 4 a,e,i) Bright field microscopy images, b,f,j) THG scanning maps, c,g,k) MPL scanning maps, and d,h,l) composite maps of the a-d) 3%, e-h) 5% and i-l) 6% Mn doped $\text{Cs}_3\text{Bi}_2\text{I}_9$ NCs. The scale bar is 3 μm .

the created micron-sized MPL aggregates in the 5% doped sample possibly exhibit or contain a high density of nanosized inhomogeneities such as molecular defects including the presence of new interfaces within its bulk. Indeed, rich Mn doping has been shown to promote the formation of defects or crystal subdomains within the host perovskite NC.⁴⁹ Due to the increased density of these defects within the MPL emitting aggregate, it is highly likely that the THG within its bulk could occur and perhaps, enhanced, complementing similar findings in defect rich perovskites.³⁴ Furthermore, the reduction of MPL signal levels in this sample as compared to its 1% and 3% counterparts indicated changes in the physical properties of the formed byproducts. This might be linked to the previous findings that high Mn doping levels in these perovskites encourage strong Mn-Mn coupling resulting to drastic changes in their emission features (e.g. energy transfer, quenching effects).^{50–52} Significant reduction of the MPL signals is further confirmed in the NLO maps of the 6% Mn doped sample, where the THG map solely represents the overall quality of the perovskite NC film (Fig. 4j-l). Here, THG is expected to be evident since the process is parametric.

To discuss the origin of THG activity in our perovskite-inspired NC samples, we compared the maximum THG signals from our $\text{Cs}_3\text{Bi}_2\text{I}_9$ NC films of varied Mn doping levels. To aid our discussion, we have processed the corresponding THG microscopy data and analyzed small, i.e., 30×30 pixels or $3 \text{ mm} \times 3 \text{ mm}$, regions (Fig. 5a) with reduced sample irregularities (e.g., hotspots). We found a linear dependence of the mean THG signal levels with respect to Mn doping

ratio from 0 up to 3% (Fig. 5b) suggesting that THG signal levels originating from samples at these doping levels can be reliably detected in our microscope. Furthermore, initial inspection of the scanning maps of the different samples in Fig. 5a could potentially reveal that the 5% Mn doped sample exhibits the highest average THG signals due to the presence of several clusters of hotspots within the scanning area. Since the THG signals from those regions in the 5% sample are possibly overlapping also to MPL emitting entities (Fig. 4h), these have been excluded in our analysis. For such kinds of data analysis, doing correlative THG and MPL based scanning microscopies in the same region of the sample is clearly advantageous and helpful in reducing the potential of overestimated or unwanted quantifications of the detected nonlinear signals and related conversion efficiencies in such kinds of nanomaterials. The sizes of the NCs and their aggregates are also expected to influence the THG signal efficiency. Aside from the possible Mn-Mn coupling effects, quenching of luminescence and defects formation at high doping levels, it was also found that Mn doping modulates the size of the constituent perovskite NCs, hence affecting its photoluminescence and optoelectronic properties.⁴⁴ In fact, the achievable size modulation for these Mn dopant levels is very small (i.e., <3 nm). It is therefore unlikely that the manipulation of THG in these samples are solely due to sizing effects of the individual NCs.

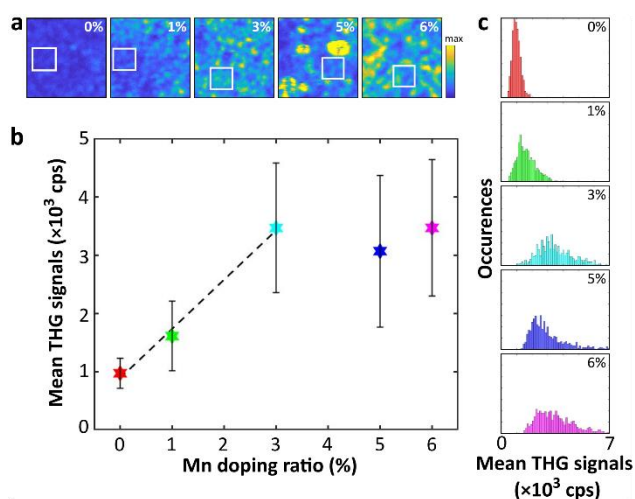


Fig 5 a) Representative THG maps from the Mn doped samples plotted in the same intensity scale. The analyzed subregions are marked by a square. b) Mn doping dependence of THG signal of perovskite NC thin films. Mean THG values have been also obtained from corresponding histograms in c).

Since THG efficiency is strongly affected by the size of the scatterer and the focused beam, it is even more likely that the THG can be significantly modulated by the micron-sized aggregates of the $\text{Cs}_3\text{Bi}_2\text{I}_9$ NCs (Fig. 5c). Most importantly, it is worth recalling that THG is highly sensitive and even modulated by interfaces between two materials where the effectively local third-order susceptibility arises from molecular-level packing symmetries even for the isotropic case.⁵³ Previous assessment of Mn doping effects to these perovskite NC samples further revealed the evolution of individual NC shape from a regular hexagon with rounded edges likely due to the CsI phase (undoped), to anisotropic or asymmetric hexagon (5%).⁴⁴ In the former, the interaction of neighboring NCs within an aggregate is moderate since the interfaces between each NC are not well-defined

so THG, although driven, could be moderate. For the latter, enhanced THG could be associated to the well-defined interfaces where the local third-order susceptibility is likely higher as well. However due to these interrelated factors, it is still difficult to pinpoint now the exact origin of THG from these materials without

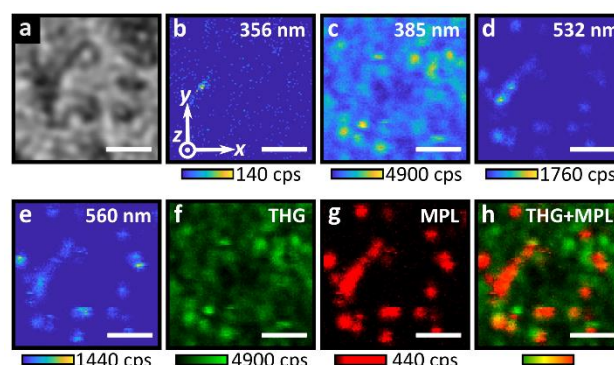


Fig 6 a) Brightfield microscopy image of the 3% Mn doped $\text{Cs}_3\text{Bi}_2\text{I}_9$ NCs. b–e) NLO scanning maps of the same area using 1155 nm femtosecond pulsed excitation different bandpass filters. The central wavelengths of the filters are shown in the top-right. f) THG map in c) as an 8-bit green color map. g) Summed MPL map using b,d,e) as an 8-bit red color map. h) Composite map of f) and g). The scale bar is 3 μm .

performing more systematic and controlled experiments.

Aside from the relaxation of the noncentrosymmetry requirement, the contrast achieved in THG microscopy is generally wavelength independent. To demonstrate this effect, we performed NLO microscopy of a region in the 3% Mn doped $\text{Cs}_3\text{Bi}_2\text{I}_9$ NC film (Fig. 6a) using a different excitation wavelength (i.e., 1155 nm) that is produced by an optical parametric oscillator (repetition rate 80 MHz, pulse length 200 fs). As shown in Fig. 6b–e, THG was found to be only significant and validated at the expected wavelength and MPL signals from micron-sized aggregates were also detected. The THG and MPL signals were found to be not overlapping in space (Fig. 6f–h) like the previous results in the 3% Mn doped samples (Fig. 4a–d). This finding further validates that correlative THG and MPL microscopy can be used to probe reliably compositional engineering effects in perovskite NC thin films. Using broadband excitation, it is also feasible to examine the role of excitonic resonances in boosting THG in NC aggregates complementing remarkable THG enhancements found in layered perovskite derivatives.^{28,31}

Conclusions

To conclude, we demonstrated the use of correlative NLO microscopy to visualize the microscopic properties of thin films of lead-free $\text{Cs}_3\text{Bi}_2\text{I}_9$ perovskite-inspired NCs particularly in examining the impact of Mn doping. Point scanning and point detection scanning microscopy of the nonlinear signals permitted us to map the optical yet spectrally distinct THG and MPL signals in these samples. THG maps revealed directly the inhomogeneities of the film. Importantly, the THG signals from Mn doped samples were found to be strongly modulated by the amount of Mn doping. MPL maps at different spectral bands revealed the presence of micron-sized aggregates in Mn doped samples. Our correlative NLO microscopy technique and findings in emerging perovskite derivatives have direct

implications in nonlinear nanophotonics and perovskite communities. The work supports the present need to develop new, noninvasive, and multimodal ways to understand the complexity, performance and (nonlinear) optical responses of perovskites as governed by hierarchical effects in its architecture and molecular compositions. In addition, the detection and control of NLO conversion efficiencies using perovskite-based nanomaterials promote the future use of these kinds of materials as new frequency converters at the nanoscale, which are still dominated by traditional nonlinear crystals based on semiconductors and dielectric materials. With suitable ultrafast excitation sources, our multimodal NLO microscopy approach can be further expanded by including other equally interesting nonlinear imaging contrast mechanisms such second-harmonic generation and four-wave mixing to investigate and exploit many unexplored aspects of perovskites for advancing nonlinear nanophotonics.

Author Contributions

S.A.: data curation, formal analysis, data validation, investigation, methodology, visualization, writing – review & editing; M.L.: conceptualization, methodology, resources, writing – review & editing; P.V.: conceptualization, funding acquisition, resources, supervision, writing – review & editing; G.B.: conceptualization, formal analysis, funding acquisition, investigation, methodology, resources, supervision, visualization, writing – original draft, review & editing. All authors have accepted responsibility for the entire content of this manuscript.

Conflicts of interest

There are no conflicts to declare.

Acknowledgements

There are no conflicts to declare. This work is part of the Academy of Finland Flagship Programme, Photonics Research and Innovation – PREIN (No. 320165). SA thanks Jenny and Antti Wihuri Foundation (No. 00220021) and Finnish Cultural Foundation (No. 50221548) for financial support. ML thanks the Finnish Cultural Foundation (No. 00220107) for the financial support. This work was partially supported by the Wallenberg Initiative Materials Science for Sustainability (WISE) funded by the Knut and Alice Wallenberg Foundation. PV thanks Academy of Finland (No. 347772) and Jane and Aatos Erkko foundation (SOL-TECH project) for the financial support.

References

- 1 E. M. Tennyson, T. A. S. Doherty and S. D. Stranks, *Nat. Rev. Mater.*, 2019, **4**, 573–587.
- 2 J. Xue, R. Wang and Y. Yang, *Nat. Rev. Mater.*, 2020, **5**, 809–827.
- 3 N. J. Jeon, J. H. Noh, W. S. Yang, Y. C. Kim, S. Ryu, J. Seo and S. Il Seok, *Nature*, 2015, **517**, 476–480.
- 4 Q. Jiang, Y. Zhao, X. Zhang, X. Yang, Y. Chen, Z. Chu, Q. Ye, X. Li, Z. Yin and J. You, *Nat. Photonics*, 2019, **13**, 460–466.
- 5 F. Wang, S. Bai, W. Tress, A. Hagfeldt and F. Gao, *npj Flex. Electron.*, 2018, **2**, 22.
- 6 H. Horieuchi, E. Ito and D. J. Weidner, *Am. Mineral.*, 1987, **72**(3–4), 357–360.
- 7 M. I. Saidaminov, J. Kim, A. Jain, R. Quintero-Bermudez, H. Tan, G. Long, F. Tan, A. Johnston, Y. Zhao, O. Voznyy and E. H. Sargent, *Nat. Energy*, 2018, **3**, 648–654.
- 8 Y. Zhou, H. Sternlicht and N. P. Padture, *Joule*, 2019, **3**(1), 641–661.
- 9 J. S. Yun, A. Ho-Baillie, S. Huang, S. H. Woo, Y. Heo, J. Seidel, F. Huang, Y.-B. Cheng and M. A. Green, *J. Phys. Chem. Lett.*, 2015, **6**(5), 875–880.
- 10 M. Ledinský, P. Löper, B. Niesen, J. Holovský, S.-J. Moon, J.-H. Yum, S. De Wolf, A. Fejfar and C. Ballif, *J. Phys. Chem. Lett.*, 2015, **6**(3), 401–406.
- 11 T. Kirchartz, J. A. Márquez, M. Stolterfoht and T. Unold, *Adv. Energy Mater.*, 2020, **10**(26), 1904134.
- 12 G. Bautista and M. Kauranen, *ACS Photonics*, 2016, **3**(8) 1351–1370.
- 13 G. Walters, B. R. Sutherland, S. Hoogland, D. Shi, R. Comin, D. P. Sellan, O. M. Bakr and E. H. Sargent, *ACS Nano*, 2015, **9**(9), 9340–9346.
- 14 W. Chen, S. Bhaumik, S. A. Veldhuis, G. Xing, Q. Xu, M. Grätzel, S. Mhaisalkar, N. Mathews and T. C. Sum, *Nat. Commun.*, 2017, **8**, 15198.
- 15 J. Chen, K. Židek, P. Chábera, D. Liu, P. Cheng, L. Nuuttila, M. J. Al-Marri, H. Lehtivuori, M. E. Messing, K. Han, K. Zheng and T. Pullerits, *J. Phys. Chem. Lett.*, 2017, **8**(10), 2316–2321.
- 16 J. Chen, W. Zhang and T. Pullerits, *Mater. Horiz.*, 2022, **9**, 2255–2287.
- 17 Z. Cao, B. Lv, H. Zhang, Y. Lv, C. Zhang, Y. Zhou, X. Wang and M. Xiao, *J. Chem. Phys.*, 2019, **151**, 154201.
- 18 J. Yu, Z. Li, Y. Liao, C. Kolodziej, S. Kuyuldar, W. S. Warren, C. Burda and M. C. Fischer, *Adv. Opt. Mater.*, 2019, **7**, 1901185.
- 19 A. Matuhina, G. K. Grandhi, A. Bergonzoni, L. Pedesseau, R. Grisorio, S. Annurakshita, H. Ali-Löyty, R. Varghese, K. Lahtonen, G. Volonakis, V. Pecunia, G. Bautista, J. Even and P. Vivo, *Nanoscale*, 2023, **15**, 14764–14773.
- 20 C. Stavrakas, A. A. Zhumekenov, R. Brenes, M. Abdi-Jalebi, V. Bulović, O. M. Bakr, E. S. Barnard and S. D. Stranks, *Energy Environ. Sci.*, 2018, **11**, 2846–2852.
- 21 C. Stavrakas, G. Delport, A. A. Zhumekenov, M. Anaya, R. Chahbazian, O. M. Bakr, E. S. Barnard and S. D. Stranks, *ACS Energy Lett.*, 2020, **5**, 1, 117–123.
- 22 J. Xu, X. Li, J. Xiong, C. Yuan, S. Semin, T. Rasing and X.-H. Bu, *Adv. Mater.*, 2020, **32**(3) 1806736.
- 23 R. W. Boyd, *Nonlinear Optics*, Academic Press, 2008.
- 24 Y. Barad, H. Eisenberg, M. Horowitz and Y. Silberberg, *Appl. Phys. Lett.*, 1997, **70**, 922–924.
- 25 J. A. Squier, M. Müller, G. J. Brakenhoff and K. R. Wilson, *Opt. Express*, 1998, **3**, 315–324.
- 26 C.-Q. Xu, T. Kondo, H. Sakakura, K. Kumata, Y. Takahashi and R. Ito, *Solid State Commun.*, 1991, **79**, 245–248.
- 27 A. Rubino, T. Huq, J. Dranczewski, G. Lozano, M. E. Calvo, S. Vezzoli, H. Míguez and R. Sapienza, *J. Mater. Chem. C.*, 2020, **8**, 15990–15995.
- 28 F. O. Saouma, C. C. Stoumpos, J. Wong, M. G. Kanatzidis and J. I. Jang, *Nat. Commun.*, 2017, **8**, 742.
- 29 A. M. Abu Baker, G. S. Boltaev, M. Iqbal, M. Pylnev, N. M. Hamdan and Ali S. Alnaser, *Materials*, 2022, **15**, 389.
- 30 Z. Chen, Q. Zhang, M. Zhu, H. Chen, X. Wang, S. Xiao, K. P. Loh, G. Eda, J. Meng and J. He, *J. Phys. Chem. Lett.*, 2021, **12**, 7010–7018.
- 31 I. Abdelwahab, G. Grinblat, K. Leng, Y. Li, X. Chi, A. Rusydi, S. A. Maier and K. P. Loh, *ACS Nano*, 2018, **12**(1), 644–650.

- 32 L. Yao, Z. Zeng, C. Cai, P. Xu, H. Gu, L. Gao, J. Han, X. Zhang, X. Wang, X. Wang, A. Pan, J. Wang, W. Liang, S. Liu, C. Chen and J. Tang, *J. Am. Chem. Soc.*, 2021, **143**(39), 16095–16104.
- 33 G. K. Grandhi, A. Matuhina, M. Liu, S. Annurakshita, H. Ali-Löytty, G. Bautista and P. Vivo, *Nanomaterials*, 2021, **11**(6), 1458.
- 34 P. Bhattacharya, M. V. Morrell, Y. Xing, C. J. Mathai, P. Yu and S. Guha, *J. Phys. Chem. Lett.*, 2021, **12**(16), 4092–4097.
- 35 S. D. Stranks, *Matter*, 2021, **4**(12), 3852–3866.
- 36 D. W. deQuilettes, S. M. Vorpahl, S. D. Stranks, H. Nagaoka, G. E. Eperon, M. E. Ziffer, H. J. Snaith and D. S. Ginger, *Science*, 2015, **348**, 683–686.
- 37 E. M. Tennyson, K. Frohna, W. K. Drake, F. Sahli, T. C.-J. Yang, F. Fu, J. Werner, C. Chosy, A. R. Bowman, T. A. S. Doherty, Q. Jeangros, C. Ballif and S. D. Stranks, *ACS Energy Lett.*, 2021, **6**(6), 2293–2304.
- 38 T. W. Jones, A. Osharov, M. Alsari, M. Sponseller, B. C. Duck, Y.-K. Jung, C. Settens, F. Niroui, R. Brenes, C. V. Stan, Y. Li, M. Abdi-Jalebi, N. Tamura, J. Emyr Macdonald, M. Burghammer, R. H. Friend, V. Bulović, A. Walsh, G. J. Wilson, S. Lilliu and S. D. Stranks, *Energy Environ. Sci.*, 2019, **12**, 596–606.
- 39 N. Li, Y. Luo, Z. Chen, X. Niu, X. Zhang, J. Lu, R. Kumar, J. Jiang, H. Liu, X. Guo, B. Lai, G. Brocks, Q. Chen, S. Tao, D.P. Fenning and H. Zhou, *Joule*, 2020, **4**, 1743–1758.
- 40 A. Merdasa, Y. Tian, R. Camacho, A. Dobrovolsky, E. Debroye, E. L. Unger, J. Hofkens, V. Sundström and I. G. Scheblykin, *ACS Nano*, 2017, **11**(6), 5391–5404.
- 41 G. Bautista, C. Dreser, X. Zang, D. P. Kern, M. Kauranen and M. Fleischer, *Nano Lett.*, 2018, **18**(4), 2571–2580.
- 42 S. Annurakshita, V. Lahti, L. Petit and G. Bautista, *Opt. Mater. Express*, 2022, **12**, 2805–2814.
- 43 L. Kallioniemi, S. Annurakshita and G. Bautista, *OSA Continuum*, 2020, **3**, 2961–2967.
- 44 M. Liu, H. Ali-Löytty, A. Hiltunen, E. Sarlin, S. Qudsia, J.-H. Smått, M. Valden and P. Vivo, *Small*, 2021, **17**(19), 2100101.
- 45 L. Liu, C. Zuo and L. Ding, *Nano Energy*, 2021 **90**, 106509.
- 46 N. Pradhan, *J. Phys. Chem. Lett.*, 2019, **10**(10), 2574–2577.
- 47 A. K. Guria, S. K. Dutta, S. D. Adhikari and N. Pradhan, *ACS Energy Lett.*, 2017, **2**(5), 1014–1021.
- 48 S. Zou, Y. Liu, J. Li, C. Liu, R. Feng, F. Jiang, Y. Li, J. Song, H. Zeng, M. Hong and X. Chen, *J. Am. Chem. Soc.*, 2017, **139**, 11443.
- 49 S. Paul, E. Bladt, A. F. Richter, M. Döblinger, Y. Tong, H. Huang, A. Dey, S. Bals, T. Debnath, L. Polavarapu and J. Feldmann, *Angew. Chem. Int. Ed. Engl.*, 2020, **59**(17), 6794–6799.
- 50 X. Zhu, S. Meng, Y. Zhao, S. Zhang, J. Zhang, C. Yin and S. Ye, *J. Phys. Chem. Lett.*, 2020, **11**, 9587–9595.
- 51 T. Qiao, D. Parobek, Y. Dong, E. Ha and D. H. Son, *Nanoscale*, 2019, **11**, 5247–5253.
- 52 Y. Liu, J. Zhang, B. Han, X. Wang, Z. Wang, C. Xue, G. Bian, D. Hu, R. Zhou, D.-S. Li, Z. Wang, Z. Ouyang, M. Li and T. Wu, *J. Am. Chem. Soc.*, 2020, **142**(14), 6649–6660.
- 53 G. Bautista, S. G. Pfisterer, M. J. Huttunen, S. Ranjan, K.a Kanerva, E. Ikonen and M. Kauranen, *Biophys. J.*, 2014, **107**(10) 2230–2236.